Field-scale Soil Moisture Retrieval from Drone-based L-band Radiometry with Optical and Thermal Infrared Priors

Zixi Li[1,2], Yan Li[3], Rui Tong[2,4*], Peizhe Cheng[1,2], Fuqiang Tian[1,2,4], Yao Zhuang[4,5]

[1]Department of Hydraulic Engineering, Tsinghua University, Beijing 100084, China

[2]State Key Laboratory of Hydroscience and Engineering, Tsinghua University, Beijing 100084, China

[3]Information Center (Hydrology Monitor and Forecast Center), Ministry of Water Resources, Beijing 100053, China

[4]Fujian Key Laboratory of Severe Weather & Key Laboratory of Straits Severe Weather, China Meteorological Administration, Fuzhou 350008, China

[5]Fujian Meteorological Administration, Fuzhou 350008, China

Correspondence to: Rui Tong (tongrui@tsinghua.edu.cn)

Abstract. Accurate field-scale near-surface soil moisture is essential for infiltration, runoff generation, land-atmosphere exchange, and agricultural water management. Drone-based low-frequency (L-band) radiometry offers a promising intermediate scale between in situ measurements and satellite observations, but retrieval remains ill-posed because brightness temperature depends jointly on soil dielectric properties, vegetation attenuation, surface temperature, and sub-footprint heterogeneity. This study develops an uncertainty-aware Bayesian retrieval framework that integrates unmanned aerial vehicle (UAV) dual-polarized L-band brightness temperature with red-green-blue (RGB) and thermal infrared (TIR) information through footprint-consistent priors. Optical fraction vegetation cover, thermal state, and texture descriptors are used to constrain vegetation optical depth (τ) and its uncertainty at the scale of the radiometric footprint. The method was evaluated over heterogeneous cropland in Pengzhou, China, using independent calibration (4 scenes, about 1.3 ha) and validation datasets (13 scenes, about 12.6 ha). The proposed approach reduced root mean square error (RMSE) from about 0.057 to about 0.024 m^3 m^{-3} and largely eliminated the systematic dry bias of the conventional τ–ω inversion. The uncertainty diagnostics showed that footprint-scale texture was more strongly associated with τ-related uncertainty than with posterior soil-moisture variance or absolute retrieval error. Overall, the results indicate that physically informed multi-source priors can improve both accuracy metrics and interpretability for field-scale hydrological soil-moisture observation.

1. Introduction

Soil moisture regulates energy partitioning, infiltration and runoff processes, and plant water use, making it a key state variable in hydrology and land-atmosphere interactions (Su et al., 2014; Li, Migliavacca et al., 2022; Wang et al., 2024). Satellite passive microwave missions such as SMOS and SMAP have established L-band radiometry as a physically meaningful approach for large-scale soil moisture monitoring due to its sensitivity to near-surface dielectric properties and reduced influence from vegetation (Kerr et al., 2010; Meyer et al., 2022; Jääskeläinen et al., 2025).

Unmanned aerial vehicle (UAV)-borne L-band radiometry offers a useful middle scale between plot measurements and satellites. Compared with satellite sensors, drone platforms provide much finer spatial resolution, more flexible acquisition timing, and better control over repeat surveys. The PoLRa platform is one example of a portable L-band system designed for field deployment and UAV integration (Houtz et al., 2020). Recent studies have shown that portable or UAV-compatible L-band radiometers can retrieve meaningful soil moisture under both bare and vegetated conditions, and can be used to test retrieval concepts before transfer to coarser airborne or spaceborne applications (Zhang et al., 2024; Lv et al., 2024; Krishnan and Indu, 2025; Wang et al., 2024).

However, high spatial resolution does not remove the core inversion difficulty of passive microwave retrieval. L-band brightness temperature still integrates multiple physical controls, including soil dielectric properties, vegetation attenuation, single-scattering albedo, soil surface temperature, and local roughness. In practice, the τ–ω forward model is often calibrated with simplified assumptions, and different combinations of soil moisture and vegetation optical depth can explain similar brightness temperatures. This leads to compensation effects, biased solutions, and uncertainty that is difficult to quantify when the inversion is performed with weak or static priors (Wigneron et al., 2007; Ebtehaj and Bras, 2019; Zhao et al., 2021; Li et al., 2023; Gibon et al., 2024). Related studies on error propagation in joint microwave retrievals have shown that uncertainty in vegetation terms can directly amplify soil moisture uncertainty, particularly under mixed cover conditions (Feldman et al., 2021; Lu et al., 2025). For field-scale UAV applications, where crop type can change within a short distance, these issues become even more pronounced.

Optical and thermal remote sensing provide a natural complement to L-band radiometry because they describe canopy cover, surface temperature state, and fine-scale spatial organization at a much higher resolution than the microwave footprint. RGB (Red-Green-Blue) and TIR (thermal infrared) data cannot replace L-band observations, but they can constrain the physically plausible range of vegetation attenuation and indicate whether the microwave footprint is homogeneous or internally mixed. This idea is consistent with broader optical-thermal soil moisture research. Surface temperature and energy-balance approaches can inform root-zone or shallow soil wetness patterns (Alburn et al., 2015; Sahaar et al., 2022; Gao et al., 2022), while drone-based RGB-TIR studies show that thermal and visible cues can improve field-scale soil moisture estimation under crop canopies when local structure is considered explicitly (Li, Liu et al., 2022; Shi et al., 2024; Vahidi et al., 2025). Reviews of UAV thermal remote sensing in agriculture also emphasize that thermal imagery becomes more informative when linked to canopy structure and field context rather than interpreted as a standalone moisture proxy (Messina and Modica, 2020).

Another unsolved issue is the mismatch between the coarse effective support of L-band radiometry and the much finer support of RGB and thermal products. Even at low UAV altitudes, the radiometric footprint remains several meters wide, so the observed brightness temperature represents an area-integrated signal rather than a point measurement (Gruber et al., 2020). When the footprint contains mixed crops, exposed soil, or strong small-scale thermal contrasts, the inversion becomes a nonlinear averaging problem, for which retrieval from averaged brightness temperature is not equivalent to averaging pointwise retrievals. Previous studies have shown that such sub-pixel heterogeneity can distort passive microwave soil moisture retrievals, with errors depending on vegetation and land-cover contrasts within the support area (Burke and Simmonds, 2003; Lakhankar et al., 2009; Barrée et al., 2021). In addition, the effective sensing depth of L-band radiometry is itself moisture-dependent, further complicating the relationship between surface measurements and footprint-scale observations (Escorihuela et al., 2010; Shen et al., 2021).

Recent studies have increasingly addressed scale mismatch in soil moisture retrieval by combining microwave observations with high-resolution optical, thermal, or spatial-context information. Operational τ–ω satellite algorithms are physically interpretable but remain limited by coarse footprints and simplified vegetation assumptions, whereas empirical or machine-learning fusion methods can exploit fine-scale auxiliary data but often depend on site-specific training and scale-consistent calibration (Peng et al., 2017; Zhong et al., 2024; Vahidi et al., 2025). However, existing approaches still rarely incorporate high-resolution RGB-TIR information into a UAV L-band retrieval in a way that is explicitly matched to the microwave footprint and accompanied by posterior uncertainty quantification.

This study addresses these challenges by developing an uncertainty-aware Bayesian joint retrieval framework that integrates UAV L-band radiometry with RGB and thermal infrared information, explicitly accounting for footprint-scale heterogeneity. The approach has three key advances. First, it introduces physically informed priors, in which RGB-TIR features constrain vegetation optical depth and temperature-related states in a scene-dependent manner. Second, it formulates the retrieval as an uncertainty-aware inversion, enabling joint estimation of soil moisture and posterior uncertainty. Third, it incorporates footprint-consistent texture integration, ensuring that high-resolution optical and thermal information is aggregated in a manner consistent with the radiometric support.

The framework is evaluated over heterogeneous agricultural fields in the Pengzhou irrigation district, Sichuan Province, using independent calibration and validation datasets. This design allows us to assess not only retrieval accuracy, but also how footprint-scale heterogeneity metrics are associated with retrieval uncertainty and representation error. In this way, the study provides a physically interpretable pathway for improving field-scale soil moisture estimation and its use in hydrological analysis under heterogeneous land-surface conditions.

2. Materials and Methods

2.1 Study Area and Observation Targets

The study area is located in Pengzhou irrigation district, Sichuan Province, China, on the northwestern margin of the Chengdu Plain (31.0°N, 103.9°E) shown in Figure 2 (a-b). The region has a humid subtropical monsoon climate, characterized by abundant precipitation, frequent rainfall events during the growing season, and relatively high soil moisture variability. The region is an intensively managed agricultural landscape with relatively flat terrain and mixed land use. The campaign focused on cropland parcels containing wheat, garlic, bare soil, rapeseed, lettuce, maize, and rice. According to field notes and local land-use context, the cultivated soils are dominated by paddy-derived and alluvial agricultural soils that are typical of irrigated plains in the basin margin. The target variable of the study was volumetric surface soil moisture. Scene boundaries and field positions were recorded in campaign geospatial files and were used together with orthomosaics and GPS information for scene registration and validation.

The chosen landscape is suitable for testing the proposed framework because it combines moderate regional uniformity with strong field-scale variability. Adjacent parcels often differ in canopy cover, row structure, irrigation history, and exposed soil fraction. This creates local contrasts in vegetation optical depth, surface temperature, and sub-footprint heterogeneity. From a retrieval perspective, these differences challenge any inversion that assumes one homogeneous land surface inside the radiometric support area. From an application perspective, they reflect the actual conditions faced by precision agriculture and smallholder field management in the Chengdu Plain.

2.2 UAV Remote-Sensing System

Two UAV sensing systems were used. The microwave observations were acquired with a DJI Matrice 600 platform carrying the PoLRa v3.1 drone-mounted portable L-band radiometer. PoLRa operates at approximately 1.4 GHz, records dual-polarized brightness temperatures, and is designed for field deployment where a lightweight, portable radiometric package is needed (Houtz et al., 2020). The use of dual polarization is important because the joint response of horizontal and vertical channels improves sensitivity to soil dielectric conditions while still retaining information on vegetation attenuation and scene thermal state.

High-resolution optical and thermal data were acquired with a DJI Mavic 2 Enterprise Advanced. The visible sensor provided RGB imagery for orthomosaics, vegetation fraction proxies, and luminance-based texture analysis, while the thermal sensor provided surface temperature patterns and thermal texture descriptors.

Brightness temperatures in horizontal and vertical polarization (TBH and TBV) were obtained from the system-level radiometric processing of the PoLRa instrument and then screened for physically implausible values, unstable attitude, and poor spatial matching. Incidence-angle consistency was controlled mainly by the fixed sensor mounting, low-altitude flight design, and attitude screening. The exact radiometric uncertainty of individual TBH/TBV samples was not independently quantified during this campaign; residual radiometric and incidence-angle uncertainty is represented in the retrieval by the microwave likelihood spread and retained as a measurement-noise limitation.

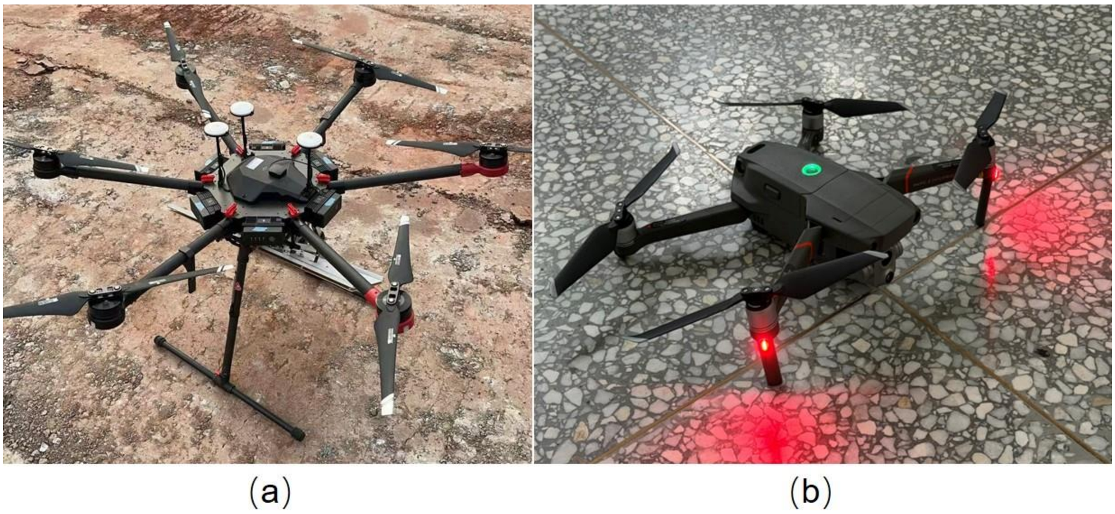

Figure 1. Field deployment of the UAV sensing system, including the (a) DJI Matrice 600 platform carrying the PoLRa v3.1 dual-polarized L-band radiometer and the (b) DJI Mavic 2 Enterprise Advanced used for RGB-TIR survey.

2.3 Flight Experiment Design and Ground Data Collection

The PoLRa flights were conducted at approximately 6 m above ground with a nominal incidence angle of 40°. According to the PoLRa hardware design described by Houtz et al. (2020), this flight geometry corresponds to an effective microwave footprint of about 4 m × 7 m. We therefore used a heading-oriented ellipse of this nominal size for footprint-scale aggregation, while treating it as a geometry-informed approximation of effective support rather than a measured antenna-pattern-weighted footprint. The 5 m × 5 m square experiment was used to evaluate sensitivity to an alternative, similarly sized footprint representation; it does not quantify uncertainty in the exact antenna response. The RGB-TIR flights were conducted at approximately 25 m, with 80% forward overlap and 70% side overlap. The resulting products reached an optical ground resolution of about 8 mm and a thermal resolution of roughly 10 cm after mosaicking. These settings provided sufficient detail to summarize sub-footprint structure while still covering each scene efficiently.

Reference soil moisture was measured using a portable time-domain reflectometry (TDR) probe (HydraGO, Stevens Water Monitoring Systems, USA). At each sampling location, repeated probe readings were averaged to reduce point-scale noise. For validation, TDR observations were matched to the effective microwave support rather than to a single point. Ground measurements falling within the assumed radiometric footprint were averaged to form footprint-scale validation labels. The heading-oriented 4 m × 7 m ellipse was used as the primary footprint, while the 5 m × 5 m square was used in the footprint-representation sensitivity test. This aggregation reduces support mismatch with the L-band observation, although it inevitably smooths some point-scale variability. High-resolution RGB and TIR data remain useful after this validation aggregation because they preserve sub-footprint structure, allowing vegetation fraction, thermal state, and texture descriptors to be summarized over the microwave footprint rather than sampled at a single pixel.

The calibration subset consisted of four scenes collected on 2026-04-03, covering approximately 1.3 ha and 52 calibration points. The independent validation subset was based on repeated experiments conducted over five days (2026-04-04, 2026-04-05, 2026-06-01, 2026-06-02, and 2026-06-03), collectively covering approximately 12.6 ha of agricultural land and 219 matched validation points. Rainfall events of approximately 3 mm and 4 mm occurred in the early hours of 2026-04-05 and 2026-06-02, respectively. All experimental observations were conducted between 11:00 and 16:00 local time. Selected representative measurement transects and ground sampling points are shown in Figure 2.

All remote-sensing products were aligned in a common spatial frame using GPS information and manual co-registration checks. The RGB and thermal images were mosaicked, and the thermal products were converted to temperature layers using the available DJI thermal processing workflow; no independent field emissivity calibration was available. Accordingly, the thermal data were used mainly as relative scene-level temperature and texture information, with thermal calibration and emissivity uncertainty retained as limitations. The microwave flight lines were screened using TBH/TBV plausibility, attitude, and co-registration checks before interpolation to scene grids for visualization and point matching. Because the support area of the L-band radiometer is larger than the RGB-TIR pixel support, optical and thermal variables were summarized inside the assumed microwave footprint rather than sampled at a single pixel. This preprocessing, footprint-consistent aggregation, Bayesian retrieval, validation, baseline comparison, and uncertainty evaluation are summarized in Figure 3.

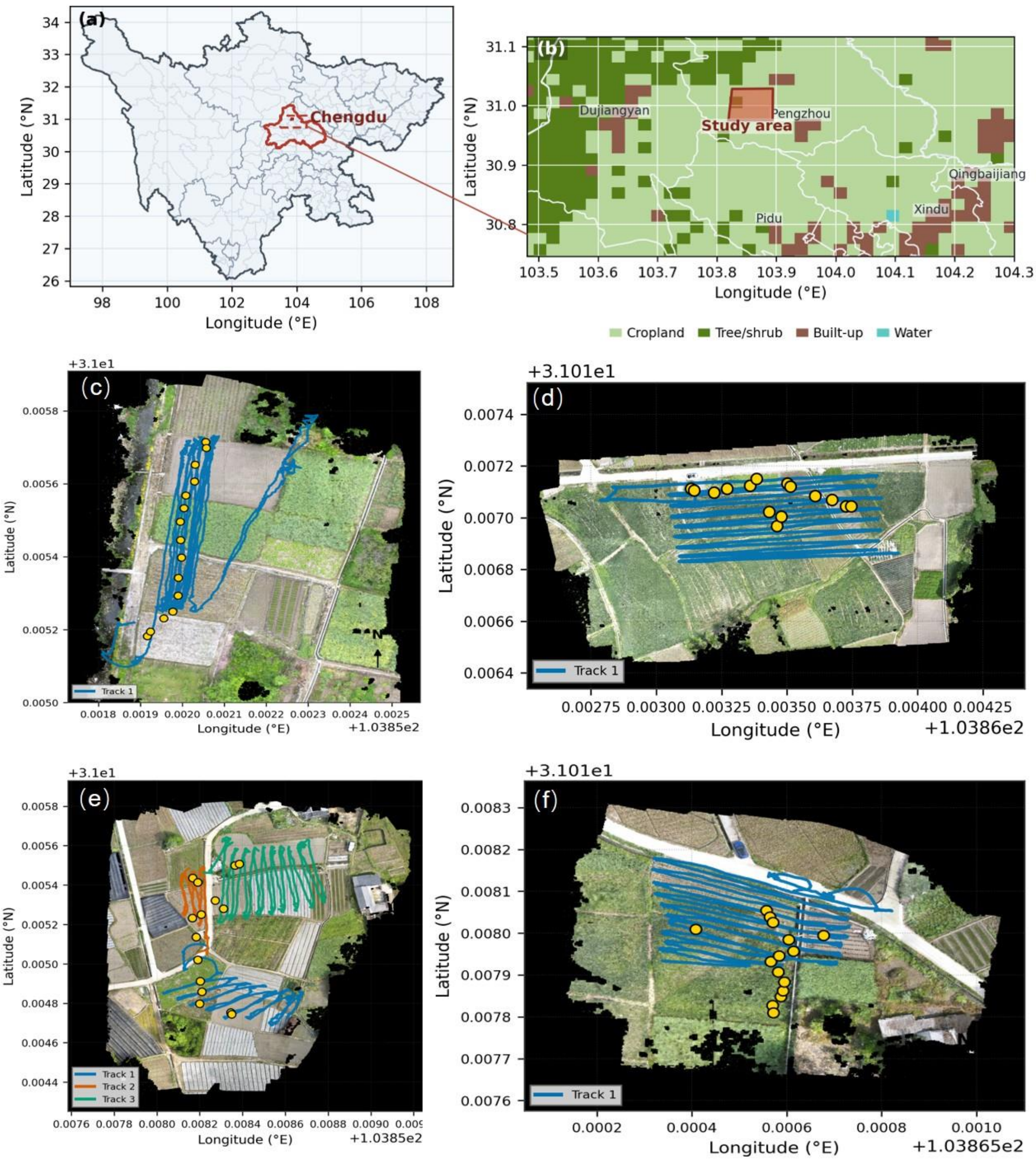

Figure 2. Study location and validation layout in Pengzhou, Chengdu Plain, Sichuan Province, China. Panels (a-b) show the regional and field locations; panels (c-f) show representative partial RGB orthomosaic backgrounds with UAV flight tracks and in situ soil-moisture measurement points. Blue lines denote flight tracks, and yellow circles denote in situ soil-moisture measurement locations.

2.4 Soil Moisture Retrieval Algorithm

The whole framework of the algorithm is shown in Figure 3 (a). The retrieval core is the dual-polarized τ–ω emission model. For polarization p, the brightness temperature can be written as:

$$TB_p = T_g[(1-\omega)(1-\Gamma)(1+r_p\Gamma)+(1-r_p)\Gamma] \quad (1)$$

where Tg is the effective ground or vegetation-soil composite temperature, ω is the single-scattering albedo, r_p is the soil reflectivity at polarization p, and $\Gamma = \exp(-\tau / \cos\theta)$ is the canopy transmissivity with optical depth τ and incidence angle θ. The reflectivity term is linked to the complex dielectric constant through the Fresnel equations, while the dielectric constant is related to soil moisture with the Dobson mixing model (Dobson et al., 1985). Equation (1) is standard in L-band passive microwave retrieval and forms the physical backbone of both the baseline and the proposed methods (Wigneron et al., 2007).

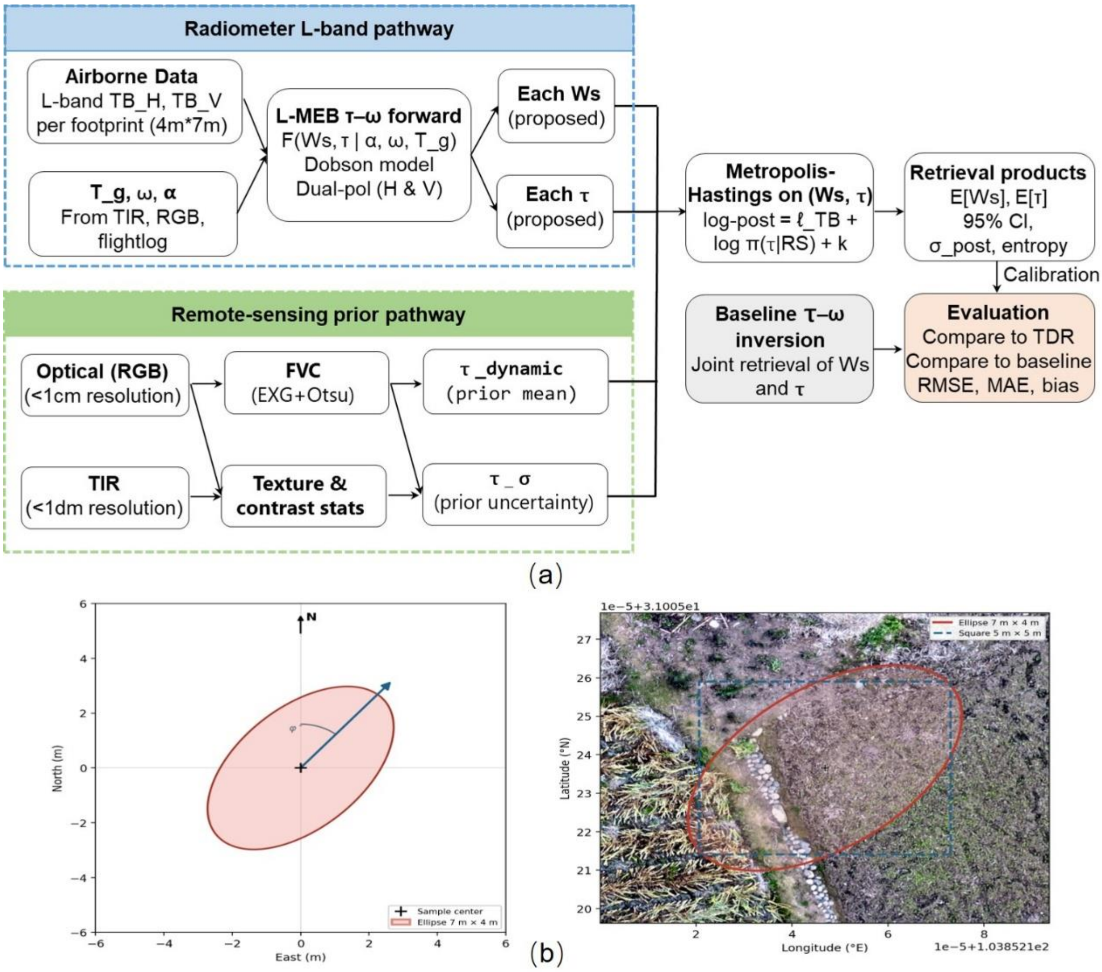

Figure 3. Workflow of the Bayesian joint retrieval. The workflow includes data preprocessing, radiometric brightness-temperature quality control, footprint-consistent RGB-TIR aggregation, Bayesian retrieval with RGB-TIR-informed priors, TDR validation labels, baseline comparison, and uncertainty evaluation. Panel (b) illustrates the nominal 4 m × 7 m heading-oriented ellipse used as a geometry-informed approximation of microwave support when summarizing high-resolution optical and thermal information before Bayesian inversion.

The effective temperature Tg was treated as a sample-wise vegetation–soil composite temperature in the forward model. In the implementation, Tg was initialized from the sampled thermal-raster temperature when valid, or from a fallback reference temperature otherwise, and then adjusted using a bounded empirical correction: $Tg = T_{base} + \Delta T$. The correction term was defined as $\Delta T = 1.5(I - 0.5) - 1.0(FVC - 0.5) - 0.5(H - 0.5)$, with an additional safeguard bound of ± 4 K. Here, I is normalized optical intensity, FVC is fraction vegetation cover, and H is the normalized heterogeneity index. This correction was used to represent scene-level differences in effective emitting temperature rather than to provide an independently calibrated thermodynamic temperature. No independent field emissivity calibration was available; therefore, the thermal data were used as relative support for Tg and texture rather than as fully traceable absolute radiometric temperature. The single-scattering albedo was parameterized as $\omega = \text{clip}(\omega_0 + 0.03H, 0.00, 0.20)$, where ω_0 is the baseline single-scattering albedo and H is the normalized heterogeneity index. These bounds were used to prevent nonphysical solutions and to keep the inversion within the range supported by the calibration scenes and sensitivity tests, rather than to prescribe universal crop-independent constants. In the baseline inversion, soil moisture Ws and vegetation optical depth τ are solved jointly from the observed TBH and TBV, using fixed or weakly varying ancillary terms and no learned remote prior. This is a practical benchmark because it follows the common strategy of using the microwave observation itself to determine both dielectric and attenuation terms. However, in heterogeneous scenes this joint inversion can become under-constrained. Similar brightness temperatures may be reproduced by a wetter soil with a lower attenuation or by a drier soil with a higher attenuation, especially when independent information on canopy state is limited (Ebtehaj and Bras, 2019; Zhao et al., 2021).

The proposed framework introduces a Bayesian prior pathway driven by RGB and thermal features. First, RGB orthomosaics were converted into vegetation-sensitive descriptors, including excess green and an Otsu-thresholded fraction vegetation cover term (Meyer and Neto, 2008). Second, both RGB and thermal data were summarized into footprint-scale texture descriptors. In practice, the local standard deviation of optical luminance and the local standard deviation of thermal temperature were computed inside moving windows matched to the microwave support area. These variables provide simple and robust proxies for footprint-scale dispersion in optical brightness and surface temperature, which may partly reflect internal heterogeneity caused by mixed vegetation cover, exposed soil, and thermal contrast, but they do not explicitly encode directional texture features such as row orientation or canopy-gap structure. The retrieved feature set can be written as:

$$f = [FVC, T_{opt}, T_{tir}, H] \tag{2}$$

where Topt denotes optical texture, Ttir denotes thermal texture, and H is a heterogeneity-related descriptor assembled from the footprint-scale statistics. Texture descriptors were defined as local dispersion metrics computed over a footprint-matched neighborhood. For each sample location i, a spatial window Wi was extracted to match the effective microwave support, implemented as a heading-oriented ellipse (approximately 7 × 4 m) or, when disabled, a square approximation shown in Figure 3 (b).

Optical texture was computed from the luminance channel derived from RGB imagery (L=0.2989R+0.5870G+0.1140B) (ITU-R, 2011), while thermal texture was computed from the co-registered surface temperature field. These texture descriptors were computed as the standard deviation within the footprint window.

Using the four calibration scenes, the feature vector f was mapped to a prior mean and prior uncertainty for τ:

$$\mu_{\tau,i} = \beta_0 + \beta_1 f_{c,i} \tag{3}$$

$$log\sigma_{\tau,i} = \gamma_0 + \gamma_1 H_i + \gamma_2 f_{c,i} \tag{4}$$

$$\sigma_{\tau,i} = clip[\exp(log\sigma_{\tau,i}), \sigma_{min}, \sigma_{max}] \tag{5}$$

Here, H is the footprint-scale heterogeneity descriptor. The coefficients β and γ were estimated from the calibration dataset. Calibration targets for τ were obtained by inverting the τ–ω forward model using matched in situ soil-moisture observations. Consequently, uncertainty in the calibration target follows the forward-model pathway rather than entering as an independent observation of τ. An error in TDR soil moisture changes the Dobson-model dielectric constant and soil reflectivity, and the inversion can compensate for the resulting emissivity error by shifting τ. Errors in TBH/TBV directly alter the dual-polarization residuals used to identify τ, whereas errors in Tg rescale the emission terms and can be absorbed jointly by Ws and τ. Surface-roughness assumptions affect reflectivity, and co-registration or footprint-support errors cause the microwave, RGB-TIR, and TDR data to represent different surface mixtures; both pathways can therefore bias or broaden the inversion-derived τ targets.

For the present campaign, brightness-temperature error and support mismatch between point-scale TDR observations and the several-metre microwave footprint are expected to provide the most direct first-order contributions. Co-registration and footprint representation may be particularly important in mixed-canopy scenes, whereas roughness-related error may be relatively more important over exposed soil. Temperature-related error is constrained partly by the bounded Tg correction, but its contribution was not independently quantified. Because independent antenna-pattern, roughness, and absolute thermal-calibration measurements were unavailable, these expected relative effects are qualitative and should not be interpreted as a formal ranking or variance decomposition.

The fitted prior-width term can absorb part of the empirical dispersion in the inversion-derived τ targets, but it does not explicitly propagate or separate the individual measurement, ancillary-variable, support-matching, and model-structure errors. The final posterior uncertainty is therefore conditional on the calibrated prior pathway and the adopted forward-model assumptions.

In the implementation, these scene-dependent estimates were stored as sample-wise variables and used together with auxiliary fields such as effective temperature, vegetation fraction, and heterogeneity level. Rather than assuming a universal τ prior, the method leverages high-resolution imagery to adapt both the expected attenuation level and its associated uncertainty to each microwave sample. The prior mean is primarily controlled by vegetation fraction, while the prior uncertainty is modeled through a log-linear function of heterogeneity and vegetation conditions. This strategy is consistent with previous findings that retrieval performance improves when passive microwave inversions are constrained by physically informed priors reflecting local vegetation state (Feldman et al., 2021; Barrée et al., 2021).

The posterior distribution is then defined as the probability of plausible pairs of soil moisture Ws and vegetation optical depth τ after combining the microwave observations, the τ–ω forward model, and the RGB-TIR-informed prior:

$$p(Ws,\tau \mid TB,f) \propto p(TB \mid Ws,\tau,T_g,\omega) \cdot p(\tau \mid f) \cdot p(Ws) \quad (6)$$

with a Gaussian likelihood:

$$p(TB \mid Ws,\tau,T_g,\omega) \propto e^{[\frac{-(TB_{obs}-TB_{mod})^2}{(2\sigma_{TB}{}^2)}]} \quad (7)$$

and a feature-informed prior:

$$\tau \mid f \sim N(\mu_\tau(f),\sigma_\tau{}^2(f)) \quad (8)$$

The soil moisture prior was weak and mainly used to keep the solution within the physically admissible range. Posterior inference means estimating the set of plausible Ws and τ pairs that are consistent with the observed horizontal and vertical brightness temperatures (TBH and TBV), the forward model, and the feature-informed τ prior. Metropolis-Hastings Markov chain Monte Carlo (MCMC) sampling was used to sample this posterior distribution rather than returning only a single optimized solution. The sampler used multiple independent chains, bounded random-walk proposals, burn-in removal, retained posterior samples, acceptance-rate screening, and chain-length sensitivity checks; the settings and diagnostics are reported in Table S1.

2.5 Accuracy Evaluation and Baseline Comparison

Accuracy was evaluated using root mean square error (RMSE), mean absolute error (MAE), and bias, which quantify error magnitude and systematic deviation relative to the validation measurements. Bayesian retrieval uncertainty was evaluated separately using posterior standard deviation and 95% posterior credible intervals for soil moisture, which describe the spread of plausible estimates conditional on the forward model, brightness-temperature observations, and RGB-TIR-informed priors. The reported posterior intervals are conditional on the selected forward model, likelihood, and calibrated prior pathway; they do not include separately propagated uncertainty from the inversion-derived τ calibration targets.

The independent validation used experiments from 13 different scenes (about 12.6 ha, 219 validation points). Calibration was performed exclusively on four scenes (about 1.3 ha, 52 calibration points) collected on 2026-04-03. The calibrated hyperparameter settings were selected using the calibration scenes, with RMSE as the primary criterion and posterior behaviour and physical bounds used as diagnostic checks; the independent validation dataset was then used only for evaluation. The calibration dataset included bare soil, garlic, and wheat fields, while the validation dataset included bare soil, garlic, rapeseed, wheat, maize, rice and lettuce fields.

The principal baseline was a Dobson-based dual-parameter τ–ω inversion that jointly solved soil moisture and vegetation optical depth without using RGB-TIR-informed Bayesian priors. To identify the contribution of each information source, we further evaluated three progressively constrained configurations using the same calibration-validation split and retrieval settings. The +FVC configuration used fraction vegetation cover to constrain the τ prior mean, while the TIR and texture terms were disabled. The +FVC+TIR configuration additionally used the thermal-raster-based effective-temperature support, but did not include footprint-scale texture descriptors.

For the validation metrics, 95% bootstrap confidence intervals were computed by resampling matched validation points. For the Bayesian retrieval, RMSE, MAE, and bias were calculated from posterior-mean (Ws) estimates, and their bootstrap intervals describe finite-sample uncertainty in the overall metrics rather than posterior uncertainty of individual retrievals.

Additional analyses were performed by land-cover class, by footprint representation, by the relationship between texture and retrieval uncertainty, and by key-parameter sensitivity.

3. Results

3.1 Overall retrieval performance and component-wise comparison

The component-wise comparison in Figure 4 shows that the proposed Bayesian joint retrieval substantially improved independent validation performance relative to the baseline across all 219 matched validation points. The conventional baseline produced RMSE = 0.057 $m^3\ m^{-3}$, MAE = 0.052 $m^3\ m^{-3}$, and bias = -0.050 $m^3\ m^{-3}$, indicating a clear systematic dry bias. Introducing the fraction vegetation cover (FVC) prior reduced the errors to RMSE = 0.037 $m^3\ m^{-3}$ and MAE = 0.033 $m^3\ m^{-3}$, while shifting the bias to 0.012 $m^3\ m^{-3}$. Further adding TIR information slightly improved the results, with RMSE = 0.033 $m^3\ m^{-3}$, MAE = 0.031 $m^3\ m^{-3}$, and bias = -0.006 $m^3\ m^{-3}$. The full configuration, which combines FVC, TIR information, and footprint-scale texture descriptors, achieved the best overall performance, with RMSE = 0.024 $m^3\ m^{-3}$, MAE = 0.020 $m^3\ m^{-3}$, and bias = 0.008 $m^3\ m^{-3}$.

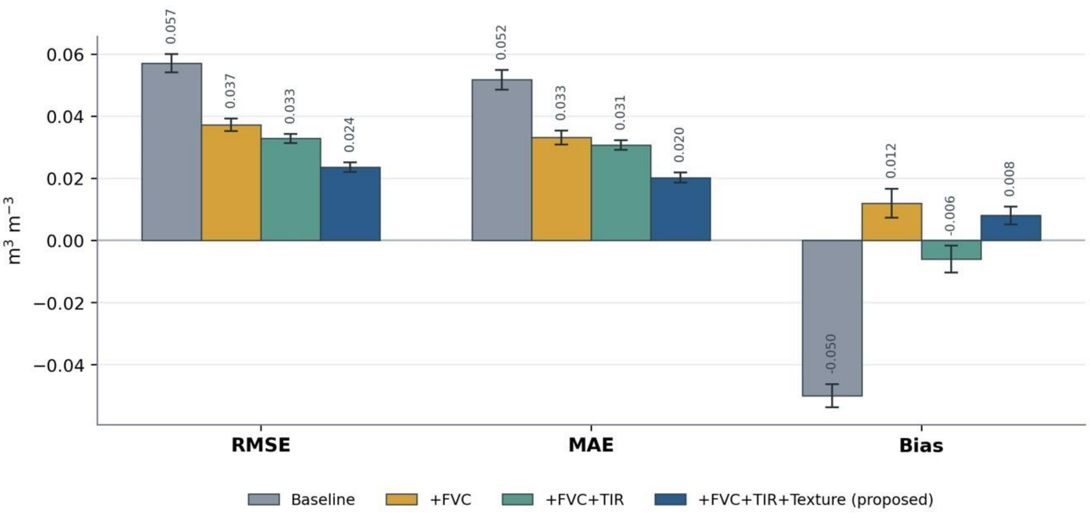

Figure 4. Component-wise comparison of validation accuracy for the baseline inversion and three

progressively constrained retrieval configurations. The four configurations are the conventional baseline, the retrieval with fraction vegetation cover (+FVC), the retrieval with both fraction vegetation cover and thermal infrared information (+FVC+TIR), and the full proposed configuration with FVC, TIR, and footprint-scale texture descriptors (+FVC+TIR+Texture). Error bars denote 95% bootstrap confidence intervals computed by resampling matched validation points.

These results indicate that the improvement was not caused by a single correction term, but was associated with the progressive introduction of physically relevant auxiliary information. The largest first-order improvement occurred after adding FVC. This pattern is consistent with vegetation-related attenuation being one contributor to ambiguity in the unconstrained τ–ω inversion, although the ablation does not isolate a unique physical mechanism. The additional gains from TIR information and footprint-scale texture descriptors were more modest, but they are consistent with the added constraints on surface thermal state and sub-footprint heterogeneity. Overall, the full RGB-TIR-texture prior pathway markedly reduced the dry bias of the baseline and improved both RMSE and MAE, supporting the value of incorporating footprint-consistent optical and thermal information into the Bayesian retrieval framework.

The retrieved-versus-observed scatter plots in Figure 5 provide a point-level evaluation of retrieval performance. The baseline retrieval is systematically shifted below the 1:1 line, especially at moderate to high soil-moisture levels, consistent with its dry bias of -0.050 $m^3 m^{-3}$. In contrast, the proposed retrieval is more closely distributed around the 1:1 line, with lower RMSE and MAE and a higher correlation coefficient than the baseline (R = 0.941 versus 0.917). The remaining slight wet bias (0.008 $m^3 m^{-3}$) and residual spread may reflect remaining effects of sub-footprint heterogeneity and support mismatch in some individual retrievals.

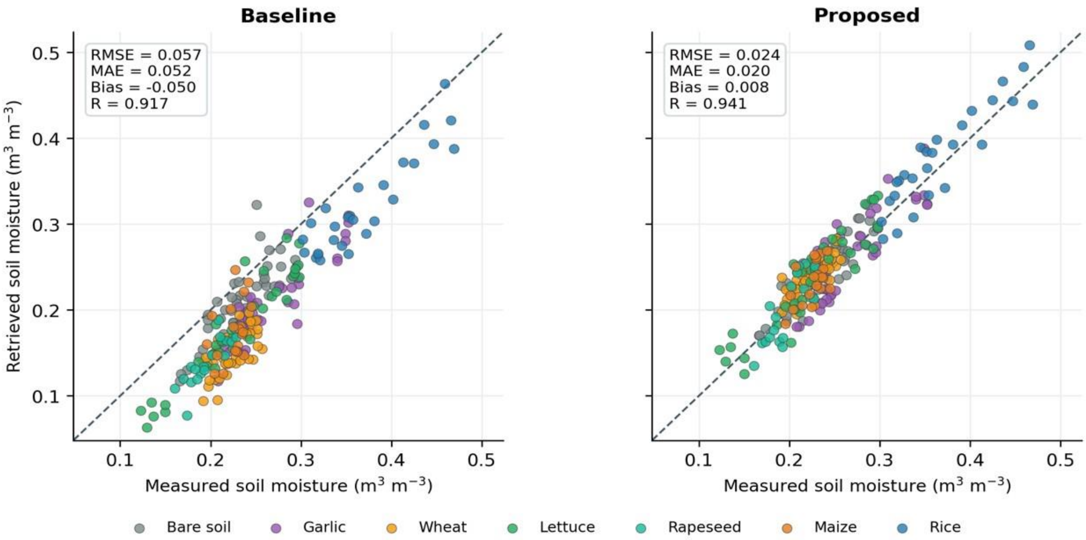

Figure 5. Retrieved versus observed surface soil moisture for the baseline inversion and the proposed Bayesian joint retrieval. The 1:1 line indicates unbiased retrieval, and points represent matched validation observations grouped by land-cover class.

Figure 6 presents representative retrieval maps overlaid on optical orthomosaics for two moisture states, with panels (a-d) corresponding to relatively drier conditions on 2026-04-04 and panels (e-h) corresponding to wetter conditions on 2026-04-05 after the early-morning rainfall event. In both cases, the proposed retrieval preserves broad field-scale soil-moisture patterns while reducing the pronounced dry shift visible in the baseline maps. Under drier conditions, the proposed product maintains spatial gradients without collapsing toward unrealistically low values, whereas under wetter conditions it reflects the overall wetter state while remaining coherent with field boundaries and within-field structure. The comparison is intended as a representative spatial visualization; quantitative validation is provided by the point-based metrics and scatter plots in Figures 4 and 5.

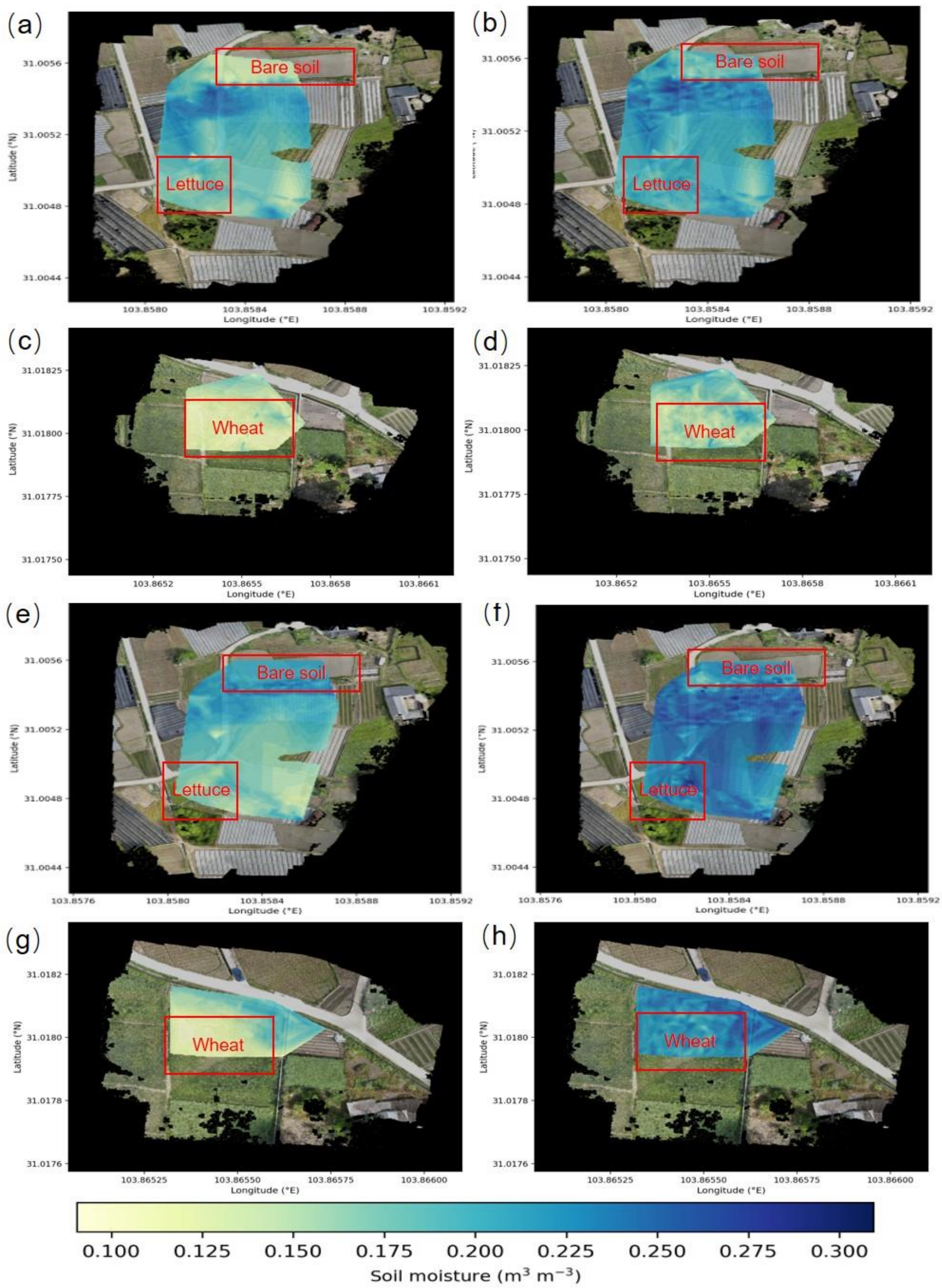

Figure 6. Representative soil moisture maps overlaid on optical orthomosaics. Panels (a-d) correspond to 2026-04-04 (relatively dry conditions) and panels (e-h) to 2026-04-05 (post-rainfall, relatively wet conditions). Panels (a, c, e, g) show the baseline retrieval, and panels (b, d, f, h) show the proposed Bayesian joint retrieval. In each group, panels for the baseline retrieval and proposed Bayesian joint retrieval use a common soil-moisture color scale to support direct visual comparison.

3.2 Retrieval performance under varying land cover

Land-cover stratification shows that the gain of the proposed method was class-dependent but generally positive across the validation categories. Table 1 reports the sample size n and 95% bootstrap confidence intervals for each land-cover class. The largest absolute RMSE reductions occurred for wheat (0.076 to 0.020 $m^3\ m^{-3}$, n = 38) and maize (0.058 to 0.021 $m^3\ m^{-3}$, n = 20), while bare soil improved from 0.034 to 0.020 $m^3\ m^{-3}$ (n = 45). Lettuce, garlic, rapeseed, and rice also improved, although the smaller sample sizes in rapeseed and maize mean that class-specific conclusions should be interpreted with the reported confidence intervals in mind. Overall, the proposed retrieval improved land-cover-specific accuracy and bias behaviour across contrasting surface conditions, without demonstrating crop-independent transferability.

Table 1. Validation accuracy by land-cover type for the baseline retrieval and the proposed Bayesian joint retrieval

Type	n	Baseline			Bayesian joint retrieval		
		RMSE	MAE	Bias	RMSE	MAE	Bias
Bare soil	45	0.034 [0.030, 0.039]	0.030 [0.025, 0.035]	-0.025 [-0.031, -0.017]	0.020 [0.017, 0.022]	0.016 [0.013, 0.020]	0.008 [0.003, 0.013]
Garlic	36	0.062 [0.055, 0.069]	0.058 [0.051, 0.065]	-0.057 [-0.065, -0.049]	0.028 [0.025, 0.031]	0.025 [0.021, 0.029]	-0.004 [-0.013, 0.006]
Wheat	38	0.076 [0.070, 0.082]	0.074 [0.068, 0.080]	-0.074 [-0.080, -0.068]	0.020 [0.016, 0.023]	0.017 [0.014, 0.020]	0.015 [0.010, 0.019]
Lettuce	35	0.052 [0.047, 0.057]	0.049 [0.043, 0.055]	-0.048 [-0.054, -0.041]	0.026 [0.022, 0.030]	0.022 [0.017, 0.026]	0.013 [0.005, 0.020]
Rapeseed	18	0.058 [0.051, 0.065]	0.056 [0.049, 0.063]	-0.056 [-0.063, -0.050]	0.024 [0.018, 0.028]	0.021 [0.015, 0.026]	0.002 [-0.009, 0.013]
Maize	20	0.058 [0.048, 0.067]	0.052 [0.040, 0.063]	-0.050 [-0.063, -0.037]	0.021 [0.015, 0.026]	0.017 [0.011, 0.022]	0.009 [0.000, 0.017]
Rice	27	0.053 [0.045, 0.060]	0.048 [0.039, 0.056]	-0.047 [-0.056, -0.038]	0.026 [0.023, 0.030]	0.024 [0.021, 0.028]	0.011 [0.002, 0.020]

Note: Values are reported in $m^3\ m^{-3}$. Brackets denote 95% bootstrap confidence intervals computed by resampling validation points within each land-cover class. Lower RMSE and MAE indicate better performance. Positive bias indicates wet overestimation, and negative bias indicates dry underestimation.

A clear pattern is that the baseline retrieval exhibited a systematic negative bias across nearly all land-cover types, whereas the proposed method substantially reduced this dry bias and in some cases slightly overcorrected it. For example, wheat and maize biases shifted from -0.074 and -0.050 m^3 m^{-3} to 0.015 and 0.009 m^3 m^{-3}, respectively. This pattern is consistent with the overall result in Figure 4, where the unconstrained baseline showed a strong dry bias and the RGB-TIR-informed retrieval reduced that bias.

The magnitude of improvement varied among land-cover classes. Wheat and maize showed large RMSE reductions, whereas lettuce, garlic, rapeseed, and rice showed more moderate improvements. These differences indicate that retrieval performance was not uniform across surface conditions. Because the land-cover classes differed in sample size, canopy structure, exposed soil fraction, and moisture state, the class-specific results should be interpreted as descriptive evidence rather than as a definitive attribution of error sources.

3.3 Texture–uncertainty relationships

Figure 7 summarizes the relationships between footprint-scale optical and thermal texture and posterior soil-moisture uncertainty, posterior τ uncertainty, and absolute soil-moisture error across the validation data.

Footprint-scale texture was more clearly associated with posterior τ uncertainty than with soil-moisture retrieval error. Optical texture, quantified as the standard deviation of optical luminance inside the assumed microwave footprint, showed a weak but significant positive relationship with posterior soil-moisture uncertainty (Spearman $\rho = 0.14$, $p = 0.035$) and a stronger relationship with posterior τ uncertainty ($\rho = 0.32$, $p = 1.4 \times 10^{-6}$). Its relationship with absolute soil-moisture error was not significant ($\rho = 0.09$, $p = 0.17$). Thermal texture was weakly related to posterior τ uncertainty ($\rho = 0.15$, $p = 0.025$), but not to posterior soil-moisture uncertainty or absolute soil-moisture error. These statistical associations identify optical texture as the more informative descriptor in this experiment, while thermal texture provided a weaker and more scene-dependent signal; they do not establish a unique physical cause.

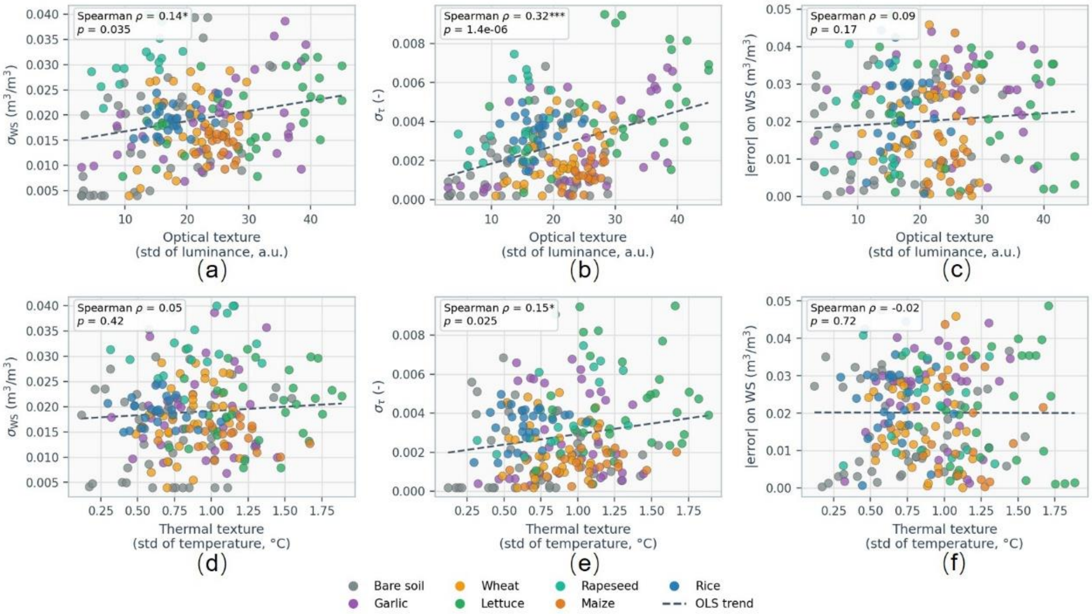

Figure 7. Relationships between footprint-scale optical and thermal texture and retrieval uncertainty. Panels (a)–(c) show optical texture versus posterior soil-moisture standard deviation, posterior τ uncertainty, and absolute soil-moisture error. Panels (d)–(f) show the corresponding thermal-texture relationships.

3.4 Sensitivity to footprint representation

The comparison between the nominal 4 m × 7 m heading-oriented ellipse and the 5 m × 5 m square is reported in Table 2. Across land-cover classes, ΔRMSE ranged from −0.002 to 0.007 $m^3\ m^{-3}$, ΔMAE from −0.002 to 0.007 $m^3\ m^{-3}$, and ΔBias from −0.001 to 0.004 $m^3\ m^{-3}$. The absolute differences were therefore small overall, indicating reasonable robustness to these two plausible footprint representations. Nevertheless, garlic, lettuce, rapeseed, and maize showed significant RMSE or MAE advantages for the ellipse, whereas bare soil and rice showed no significant RMSE difference; wheat slightly favored the square for RMSE. These class-dependent results show that the footprint approximation was not uniformly beneficial.

Table 2. Comparison of retrieval accuracy between the nominal 4 × 7 m heading-oriented ellipse and a simplified 5 × 5 m square footprint representation

Land cover	n	Δ RMSE (5x5 - 4x7)	p-value	Δ MAE (5x5 - 4x7)	p-value	Δ Bias (5x5 - 4x7)	p-value
Bare soil	45	0.001 [-0.001, 0.003]	0.395	0.001 [-0.001, 0.003]	0.513	0.000 [-0.002, 0.003]	0.763
Garlic	36	0.007 [0.004, 0.009]	<0.001***	0.006 [0.004, 0.009]	<0.001***	0.004 [0.001, 0.007]	0.017*

Land cover	n	Δ RMSE (5x5 - 4x7)	p-value	Δ MAE (5x5 - 4x7)	p-value	Δ Bias (5x5 - 4x7)	p-value
Wheat	38	-0.002 [-0.003, 0.000]	0.015*	-0.001 [-0.003, 0.000]	0.043*	-0.001 [-0.003, 0.001]	0.263
Lettuce	35	0.006 [0.003, 0.008]	<0.001***	0.006 [0.004, 0.008]	<0.001***	0.003 [0.001, 0.006]	0.011*
Rapeseed	18	0.002 [0.000, 0.003]	0.027*	0.002 [0.001, 0.003]	0.004**	0.001 [0.000, 0.003]	0.075
Maize	20	0.007 [0.002, 0.011]	0.007**	0.007 [0.002, 0.011]	0.004**	0.004 [-0.002, 0.009]	0.161
Rice	27	-0.002 [-0.005, 0.000]	0.071	-0.002 [-0.004, 0.001]	0.12	-0.001 [-0.004, 0.002]	0.436

Note: Δ values are computed as the 5 m × 5 m square result minus the 4 m × 7 m ellipse result; positive Δ therefore indicates lower error for the ellipse. Brackets denote 95% bootstrap confidence intervals. Asterisks denote significance levels (* $p < 0.05$, ** $p < 0.01$, *** $p < 0.001$).

3.5 Hyperparameter sensitivity and posterior diagnostics

The one-at-a-time sensitivity analysis in Figure 8 examined the microwave likelihood spread σTB, the scale applied to the τ prior mean, the prior-strength parameter κ, and the scale applied to the τ prior width. Across the tested ranges, validation RMSE varied moderately and the calibrated settings lay within a relatively stable neighbourhood of the response curves.

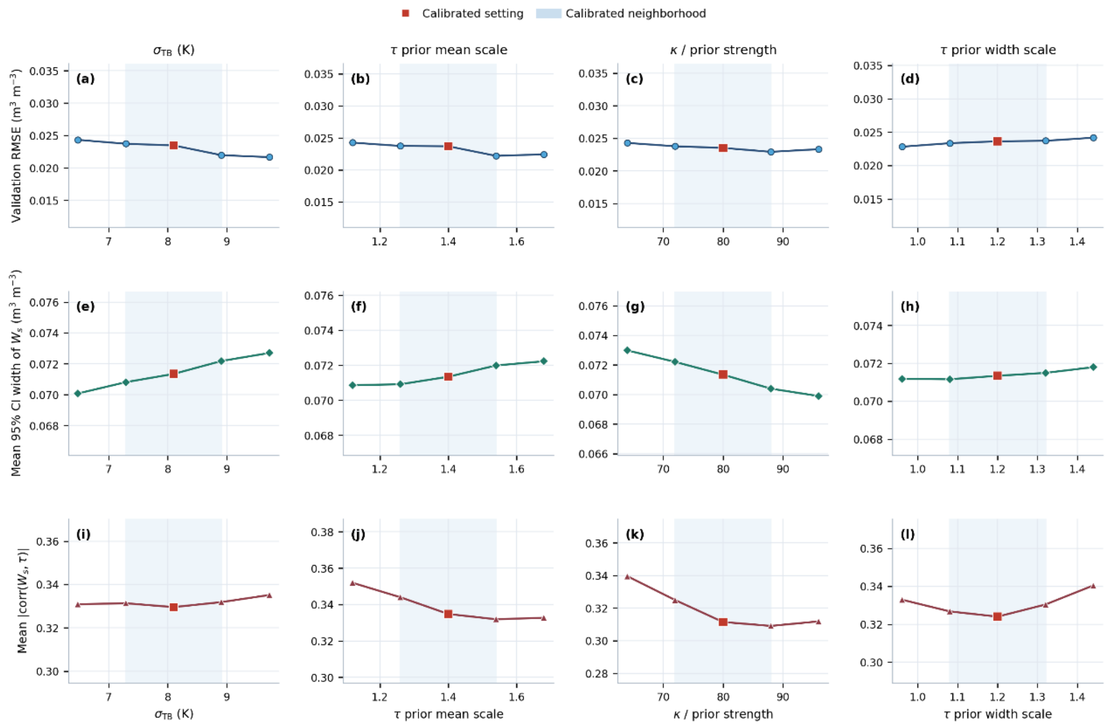

Figure 8. One-at-a-time sensitivity diagnostics for four key hyperparameters: microwave likelihood spread

σTB, τ-prior mean scale, prior strength κ, and τ-prior width scale. The first row shows validation RMSE, the second row shows the mean 95% posterior credible-interval width of Ws, and the third row shows the mean posterior correlation between Ws and τ. The credible-interval width was calculated from the 2.5^{th}–97.5^{th} percentile range of posterior Ws samples and averaged over validation points. Red squares indicate the calibrated settings, and shaded areas indicate the calibrated neighbourhood.

The mean 95% credible-interval width of Ws and the posterior correlation between Ws and τ also changed smoothly across the tested perturbations. Changes in κ and the τ-prior settings altered Ws–τ coupling without producing abrupt deterioration in RMSE. Together, these results indicate local stability around the calibrated settings, rather than insensitivity to parameter choice.

4. Discussion

4.1 Implications of sub-footprint heterogeneity and footprint representation

The L-band radiometer measures an area-integrated brightness temperature over a footprint several metres wide. When the support area contains mixed canopy density, row structure, exposed soil patches, residue, or irrigation patterns, the observed brightness temperature represents a nonlinear mixture of sub-footprint states. The inversion must then explain the aggregate signal using an effective pair of soil moisture and vegetation optical depth. Because the τ–ω forward model is nonlinear, averaging before inversion is not equivalent to inversion before averaging, which can increase ambiguity in heterogeneous scenes (Burke and Simmonds, 2003; Lakhankar et al., 2009; Chan et al., 2016). Similar effects have also been reported in L-band retrievals over heterogeneous scenes and in coupled soil-moisture and vegetation-optical-depth retrievals (Barrée et al., 2021; Feldman et al., 2021).

The stronger association of texture with τ uncertainty than with Ws error is therefore consistent with τ acting as a flexible attenuation term when multiple canopy–soil mixtures produce similar aggregate transmissivity. However, the observed associations cannot distinguish whether the pattern arose primarily from vegetation attenuation, soil–canopy mixing, support mismatch, or covarying moisture and canopy conditions. The texture metrics are proxies for broader heterogeneity, not proven causal drivers. Posterior covariance analysis, formal variance decomposition, and directional or object-based texture descriptors would be required for stronger mechanistic attribution.

The footprint-representation experiment provides a complementary robustness check. The small absolute differences between the ellipse and square suggest that the overall retrieval was reasonably robust to these two similarly sized approximations, but the significant class-specific differences show that support geometry can matter where crop rows, canopy gaps, and field boundaries are structured. The limited sensitivity of the sampled bare-soil footprints is consistent with their relatively homogeneous surface composition, so the two windows likely summarized similar reflectivity and moisture conditions. For the sampled rice plots, the two windows may likewise have contained similar water-soil-canopy proportions within comparatively continuous field units; the modest sample size ($n = 27$) also limits inference. Wheat slightly favored the square, further indicating that the nominal ellipse is not universally optimal and that row orientation, flight heading, and boundary placement may interact. These explanations are consistent with the observations but remain hypotheses rather than demonstrated mechanisms.

4.2 Retrieval robustness, parameter coupling, and calibration dependence

The smooth one-at-a-time responses in Figure 8 suggest that the calibrated solution did not depend on a single sharply tuned value within the tested neighbourhood. At the same time, changes in posterior interval width and Ws–τ correlation show that the prior and likelihood settings alter parameter coupling even when RMSE changes only modestly. Retrieval robustness should therefore be judged using both predictive metrics and posterior behaviour.

However, the analysis perturbed one parameter at a time while holding the others fixed. It supports local stability only and cannot capture global interactions, nonlinear compensation, or equifinality among σTB, the τ-prior mean, κ, and the τ-prior width. The calibrated settings should therefore be interpreted as field-scale parameters for the present dataset rather than universal values, and calibration-set dependence or overfitting cannot be excluded.

4.3 Limitations and Future Directions

Several limitations remain. The independent validation dataset includes 219 matched validation points covering approximately 12.6 ha and spans broader field conditions and cross-seasonal observations. However, all validation data were collected within the Pengzhou study area. Therefore, although the results provide a field-scale evaluation under local agricultural conditions, they should not yet be interpreted as evidence of general transferability across regions. The current experiment remains limited in terms of geographic diversity, soil background, crop-management conditions, and regional climate settings. Transfer to other regions will require additional validation across contrasting soil types, crop systems, irrigation regimes, surface roughness states, moisture regimes, and seasonal conditions, together with further testing of whether the RGB-TIR-informed priors remain stable under different environmental settings.

Another limitation concerns the vertical representativeness of the retrieved variable. The UAV L-band retrieval developed here targets surface or near-surface field-scale soil moisture, which is directly relevant to infiltration, runoff generation, evaporation partitioning, and the validation of microwave soil-moisture retrievals. However, it should not be interpreted as a direct observation of root-zone soil moisture, which is more closely linked to plant water availability and agricultural drought stress. Root-zone moisture conditions would require additional constraints, such as vegetation water indices including the Normalized Difference Infrared Index (NDII), evaporation-driven water-balance estimates of root-zone storage capacity, land-surface models, or data assimilation frameworks (Sriwongsitanon et al., 2016; Wang-Erlandsson et al., 2016; Gao et al., 2024). Therefore, the root-zone relevance of the proposed UAV L-band framework is indirect: it may provide useful near-surface constraints, but its extension to root-zone moisture estimation requires coupling with complementary hydrological or ecohydrological information.

The RGB-TIR feature pathway can also be expanded. In the present study, optical and thermal information was summarized using simple and robust descriptors, especially fraction vegetation cover and local standard-deviation texture metrics. These descriptors capture footprint-scale dispersion in optical brightness and surface temperature, and therefore provide useful first-order proxies for mixed vegetation cover, exposed soil fraction, and thermal contrast. However, they do not explicitly represent directional canopy structure, row orientation, canopy gaps, spectral variability, or viewing-geometry effects. Future work could incorporate additional texture metrics, object-based canopy descriptors, and multispectral or hyperspectral information to better separate canopy effects from soil-background effects. This direction is supported by recent optical-thermal soil moisture studies that obtained additional gains when canopy context was described more explicitly (Sahaar et al., 2022; Shi et al., 2024; Vahidi et al., 2025).

Another useful extension would be broader uncertainty partitioning. The present framework quantifies posterior uncertainty conditioned on the chosen forward model and prior pathway, but uncertainty in the inversion-derived τ calibration targets was not explicitly propagated through prior calibration into the final posterior distribution. It also does not separately decompose measurement errors, support-matching errors, and model-structure errors. These include radiometer brightness-temperature noise, TDR support mismatch, geolocation and co-registration uncertainty, footprint-shape assumptions, thermal calibration and emissivity uncertainty, vegetation-prior uncertainty, and structural simplifications in the τ–ω model. Future work could use hierarchical error models, antenna-pattern-weighted aggregation, posterior covariance analysis, or formal variance decomposition to better separate these contributions and improve the interpretability of Bayesian remote-sensing retrievals (Jing et al., 2025).

5. Conclusion

This study developed a Bayesian joint retrieval framework for drone-based L-band near-surface soil moisture estimation that integrates RGB and thermal infrared information through physically consistent, footprint-scale priors. The results indicate improved field-scale accuracy metrics and reduced dry bias relative to an unconstrained τ–ω baseline, while also indicating remaining limitations associated with sub-footprint heterogeneity and observation support mismatch.

Three main conclusions can be drawn.

(1) Incorporating RGB-TIR-informed priors significantly improved retrieval performance and reduced the systematic dry bias of the conventional τ–ω inversion, indicating the value of physically constrained auxiliary information.

(2) The texture-uncertainty analysis showed that footprint-scale texture was more clearly associated with τ-related posterior uncertainty than with absolute soil-moisture error or posterior Ws variance. This pattern is consistent with an important role for attenuation-related ambiguity, but it does not establish vegetation attenuation or canopy-soil mixing as the dominant causal mechanism.

(3) The nominal ellipse and square footprint representations produced small, class-dependent differences, with modest improvements for the ellipse in several land-cover classes. This supports matching auxiliary RGB-TIR aggregation to microwave support while showing that no single

footprint approximation was uniformly superior.

Overall, the findings suggest that improving field-scale soil moisture retrieval requires both algorithmic constraints and better representation of observation scale, surface heterogeneity, and physical processes.

The current results are based on a field-scale dataset from a single study region. Broader cross-regional validation and formal propagation of uncertainty from inversion-derived τ calibration targets, together with posterior covariance analysis or variance decomposition, are still needed before claiming general transferability or mechanistic attribution.

Appendix

Table S1. Metropolis-Hastings sampling settings and convergence diagnostics for the Bayesian joint retrieval.

Item	Setting / diagnostic
Sampler	Random-walk Metropolis-Hastings
State variables	Ws and τ
Number of chains	3 independent chains per retrieval
Iterations	1000
Burn-in	200
Retained samples	800 per chain
Initial values	Ws = 0.25; τ initialized from feature-informed prior mean; independent chains used different random seeds.
Proposal distribution	Gaussian random-walk proposal
Proposal SD for Ws	0.012 m^3 m^{-3}
Proposal SD for τ	0.006 dimensionless
Bounds for Ws	0.0–0.8 m^3 m^{-3}
Bounds for τ	0.0–1.0
Acceptance rate	Mean = 0.34, range 0.27-0.42
Convergence diagnostic	Convergence was assessed using post-burn-in trace stability, acceptance-rate screening, and consistency of posterior means and standard deviations across three independent chains.

Chain-length test	Increasing the chain length from 1,000 to 2,000 iterations produced negligible changes in validation metrics, which remained unchanged to three decimal places: RMSE = 0.024 m^3 m^{-3}, MAE = 0.020 m^3 m^{-3}, and Bias = 0.008 m^3 m^{-3}.

Glossary of abbreviations

UAV: unmanned aerial vehicle; RGB: red-green-blue imagery; TIR: thermal infrared imagery; L-band: approximately 1.4 GHz microwave frequency range; TDR: time-domain reflectometry; TBH/TBV: horizontally/vertically polarized brightness temperature; FVC: fraction vegetation cover; VOD or τ: vegetation optical depth; RMSE: root mean square error; MAE: mean absolute error; CI: confidence interval; MCMC: Markov chain Monte Carlo; Metropolis-Hastings: a random-walk sampler used to draw plausible posterior Ws and τ values.

Acknowledgments

This study has been supported by the National Natural Science Foundation of China (U2442201 & 523B1006 & 52309024), and Fujian Key Laboratory of Severe Weather & Key Laboratory of Straits Severe Weather, China Meteorological Administration (2024KFKT02).

Data availability

The running Python codes are available at Zenodo (Li, 2026).

Author contributions

ZL: Conceptualization; Data curation; Model development; Investigation; Methodology; Validation; Visualization; Writing – original draft; Writing – review & editing.

YL: Conceptualization; Investigation; Methodology; Writing – review & editing

RT: Conceptualization; Funding acquisition; Investigation; Methodology; Supervision; Writing – review & editing.

PC: Investigation; Methodology; Writing – review & editing.

FT: Funding acquisition; Methodology; Supervision; Writing – review & editing.

YZ: Investigation; Validation; Writing – review & editing.

Competing interests

At least one of the (co-)authors is a member of the editorial board of Hydrology and Earth System Sciences. The peer-review process was guided by an independent editor, and the authors also have no other competing interests to declare.

References

Alburn, N. E., Niemann, J. D., and Elhaddad, A.: Evaluation of a surface energy balance method based on optical and thermal satellite imagery to estimate root-zone soil moisture, Hydrol. Process., 29, 5354–5368, https://doi.org/10.1002/hyp.10562, 2015.

Barrée, M., Mialon, A., Pellarin, T., Parrens, M., Biron, R., Lemaître, F., Gascoin, S., and Kerr, Y.: Soil moisture and vegetation optical depth retrievals over heterogeneous scenes using LEWIS L-band radiometer, Int. J. Appl. Earth Obs. Geoinf., 102, 102424, https://doi.org/10.1016/j.jag.2021.102424, 2021.

Burke, E. J. and Simmonds, L. P.: Effects of sub-pixel heterogeneity on the retrieval of soil moisture from passive microwave radiometry, Int. J. Remote Sens., 24, 2085–2104, https://doi.org/10.1080/01431160210155938, 2003.

Chan, S. K., Bindlish, R., O'Neill, P. E., Njoku, E., Jackson, T., Colliander, A., Chen, F., Burgin, M., Dunbar, S., Piepmeier, J., Yueh, S., Entekhabi, D., Cosh, M. H., Caldwell, T., Walker, J., Wu, X., Berg, A., Rowlandson, T., Pacheco, A., McNairn, H., Thibeault, M., Martínez-Fernández, J., González-Zamora, Á., Seyfried, M., Bosch, D., Starks, P., Goodrich, D., Prueger, J., Palecki, M., Small, E. E., Zreda, M., Calvet, J.-C., Crow, W. T., and Kerr, Y.: Assessment of the SMAP passive soil moisture product, IEEE T. Geosci. Remote, 54, 4994–5007, https://doi.org/10.1109/TGRS.2016.2561938, 2016.

Dobson, M., Ulaby, F., Hallikainen, M., and El-Rayes, M.: Microwave dielectric behavior of wet soil – Part II: Dielectric mixing models, IEEE T. Geosci. Remote, GE-23, 35–46, https://doi.org/10.1109/TGRS.1985.289498, 1985.

Ebtehaj, A. and Bras, R. L.: A physically constrained inversion for high-resolution passive microwave retrieval of soil moisture and vegetation water content in L-band, Remote Sens. Environ., 233, 111346, https://doi.org/10.1016/j.rse.2019.111346, 2019.

Escorihuela, M., Chanzy, A., Wigneron, J., and Kerr, Y.: Effective soil moisture sampling depth of L-band radiometry: A case study, Remote Sens. Environ., 114, 995–1001, https://doi.org/10.1016/j.rse.2009.12.011, 2010.

Feldman, A., Chaparro, D., and Entekhabi, D.: Error propagation in microwave soil moisture and vegetation optical depth retrievals, IEEE J. Sel. Top. Appl., 14, 11311–11323, https://doi.org/10.1109/JSTARS.2021.3124857, 2021.

Gao, Y., Lian, X., and Ge, L.: Inversion model of surface bare soil temperature and water content based on UAV thermal infrared remote sensing, Infrared Phys. Techn., 125, 104289, https://doi.org/10.1016/j.infrared.2022.104289, 2022.

Gao, H., Hrachowitz, M., Wang-Erlandsson, L., Fenicia, F., Xi, Q., Xia, J., Shao, W., Sun, G., and Savenije, H. H. G.: Root zone in the Earth system, Hydrol. Earth Syst. Sci., 28, 4477-4499, https://doi.org/10.5194/hess-28-4477-2024, 2024.

Gibon, F., Mialon, A., Richaume, P., Rodríguez-Fernández, N., Aberer, D., Boresch, A., Crapolicchio, R., Dorigo, W., Gruber, A., Himmelbauer, I., Preimesberger, W., Sabia, R., Stradiotti, P., Tercjak, M., and Kerr, Y. H.: Estimating the uncertainties of satellite derived soil moisture at global scale, Sci. Remote Sens., 10, 100147, https://doi.org/10.1016/j.srs.2024.100147, 2024.

Gruber, A., De Lannoy, G., Albergel, C., Al-Yaari, A., Brocca, L., Calvet, J.-C., Colliander, A., Cosh, M., Crow, W., Dorigo, W., Draper, C., Hirschi, M., Kerr, Y., Konings, A., Lahoz, W., McColl, K., Montzka, C., Muñoz-Sabater, J., Peng, J., Reichle, R., Richaume, P., Rüdiger, C., Scanlon, T., van der Schalie, R., Wigneron, J.-P., and Wagner, W.: Validation practices for satellite soil moisture retrievals: What are (the) errors?, Remote Sens. Environ., 244, 111806, https://doi.org/10.1016/j.rse.2020.111806, 2020.

Houtz, D., Naderpour, R., and Schwank, M.: Portable L-band radiometer (PoLRa): Design and characterization, Remote Sens., 12, 2780, https://doi.org/10.3390/rs12172780, 2020.

International Telecommunication Union: Recommendation ITU-R BT.601-7: Studio encoding parameters of digital television for standard 4:3 and wide-screen 16:9 aspect ratios, International Telecommunication Union, 2011.

Jääskeläinen, E., Luoto, M., Putkiranta, P., Aurela, M., and Virtanen, T.: High-resolution soil moisture mapping in northern boreal forests using SMAP data and downscaling techniques, Hydrol. Earth Syst. Sci., 29, 6237–6256, https://doi.org/10.5194/hess-29-6237-2025, 2025.

Jing, H., Chai, L., Liu, S., Chen, D., Zhao, S., and Zhu, Z.: Improve the accuracy of SAR-based soil moisture retrieval by coupling Bayesian inference and water cloud model, J. Hydrol., 666, 134826, https://doi.org/10.1016/j.jhydrol.2025.134826, 2025.

Kerr, Y. H., Waldteufel, P., Wigneron, J. P., Delwart, S., Cabot, F., Boutin, J., Escorihuela, M. J., Font, J., Reul, N., Gruhier, C., Juglea, S. E., Drinkwater, M. R., Hahne, A., Martín-Neira, M., and Mecklenburg, S.: The SMOS mission: New tool for monitoring key elements of the global water cycle, Proc. IEEE, 98, 666–687, https://doi.org/10.1109/JPROC.2010.2043032, 2010.

Krishnan, S. and Indu, J.: Evaluating soil moisture retrieved from a portable L-band radiometer, Adv. Space Res., 75, 2018–2027, https://doi.org/10.1016/j.asr.2024.10.049, 2025.

Lakhankar, T., Ghedira, H., Temimi, M., Azar, A. E., and Khanbilvardi, R.: Effect of land cover heterogeneity on soil moisture retrieval using active microwave remote sensing data, Remote Sens., 1, 80–91, https://doi.org/10.3390/rs1020080, 2009.

Li, W., Liu, C., Yang, Y., Awais, M., Li, W., Ying, P., Ru, W., and Cheema, M. J. M.: A UAV-aided prediction system of soil moisture content relying on thermal infrared remote sensing, Int. J. Environ. Sci. Te., 19, 9587–9600, https://doi.org/10.1007/s13762-022-03958-7, 2022.

Li, W., Migliavacca, M., Forkel, M., Denissen, J. M. C., Reichstein, M., Yang, H., Duveiller, G., Weber, U., and Orth, R.: Widespread increasing vegetation sensitivity to soil moisture, Nat. Commun., 13, 3959, https://doi.org/10.1038/s41467-022-31667-9, 2022.

Li, Y., Yan, S., and Gong, J.: Quantifying uncertainty in soil moisture retrieval using a Bayesian neural network framework, Comput. Electron. Agr., 215, 108414, https://doi.org/10.1016/j.compag.2023.108414, 2023.

Li, Z.: The open code of paper titled "Bayesian joint retrieval of soil moisture from UAV L-band radiometry by integrating RGB-TIR priors and footprint-scale texture", Zenodo, https://doi.org/10.5281/zenodo.19587715, 2026.

Lu, Z., Fan, L., Liu, X., Bai, X., Baghdadi, N., Frappart, F., Zeng, J., De Lannoy, G., Peng, J., Xing, Z., Li, X., Feng, Z., Li, X., and Wigneron, J. P.: Sentinel-1 vegetation optical depth retrievals over the international soil moisture network, Int. J. Digit. Earth, 18, 2555412, https://doi.org/10.1080/17538947.2025.2555412, 2025.

Lv, S., Houtz, D., Li, S., Hu, Y., Zhang, J., Wu, D., Jin, L., and Wen, J.: Rapid retrieval of soil moisture using a novel portable L-band radiometer in the Hulunbeier Prairie, China, GISci. Remote Sens., 61, 2424337, https://doi.org/10.1080/15481603.2024.2424337, 2024.

Messina, G. and Modica, G.: Applications of UAV thermal imagery in precision agriculture: State of the art and future research outlook, Remote Sens., 12, 1491, https://doi.org/10.3390/rs12091491, 2020.

Meyer, G. E. and Neto, J. C.: Verification of color vegetation indices for automated crop imaging applications, Comput. Electron. Agr., 63, 282–293, https://doi.org/10.1016/j.compag.2008.03.009, 2008.

Meyer, R., Zhang, W., Kragh, S. J., Andreasen, M., Jensen, K. H., Fensholt, R., Stisen, S., and Looms, M. C.: Exploring the combined use of SMAP and Sentinel-1 data for downscaling soil moisture beyond the 1 km scale, Hydrol. Earth Syst. Sci., 26, 3337–3357, https://doi.org/10.5194/hess-26-3337-2022, 2022.

Peng, J., Loew, A., Merlin, O., and Verhoest, N. E. C.: A review of spatial downscaling of satellite remotely sensed soil moisture, Rev. Geophys., 55, 341–366, https://doi.org/10.1002/2016RG000543, 2017.

Sahaar, S. A., Niemann, J. D., and Elhaddad, A.: Using regional characteristics to improve uncalibrated estimation of rootzone soil moisture from optical/thermal remote-sensing, Remote Sens. Environ., 273, 112982, https://doi.org/10.1016/j.rse.2022.112982, 2022.

Shen, X., Walker, J. P., Ye, N., Wu, X., Boopathi, N., Yeo, I. Y., Zhang, L., and Zhu, L.: Soil moisture retrieval depth of P- and L-band radiometry: Predictions and observations, IEEE T. Geosci. Remote, 59, 6814–6822, https://doi.org/10.1109/TGRS.2020.3026384, 2021.

Shi, H., Liu, Z., Li, S., Jin, M., Tang, Z., Sun, T., Liu, X., Li, Z., Zhang, F., and Xiang, Y.: Monitoring soybean soil moisture content based on UAV multispectral and thermal-infrared remote-sensing information fusion, Plants, 13, 2417, https://doi.org/10.3390/plants13172417, 2024.

Sriwongsitanon, N., Gao, H., Savenije, H. H. G., Maekan, E., Saengsawang, S., and Thianpopirug, S.: Comparing the Normalized Difference Infrared Index (NDII) with root zone storage in a lumped conceptual model, Hydrol. Earth Syst. Sci., 20, 3361-3377, https://doi.org/10.5194/hess-20-3361-2016, 2016.

Susha Lekshmi, S. U., Singh, D. N., and Baghini, M. S.: A critical review of soil moisture measurement, Measurement, 54, 92–105, https://doi.org/10.1016/j.measurement.2014.04.007, 2014.

Vahidi, M., Shafian, S., and Frame, W. H.: Depth-specific soil moisture estimation in vegetated corn fields using a canopy-informed model: A fusion of RGB-thermal drone data and machine learning, Agr. Water Manage., 307, 109213, https://doi.org/10.1016/j.agwat.2024.109213, 2025.

Wang, W., Ma, C., Wang, X., Feng, J., Dong, L., Kang, J., Jin, R., and Li, X.: A soil moisture experiment for validating high-resolution satellite products and monitoring irrigation at agricultural field scale, Agr. Water Manage., 304, 109071, https://doi.org/10.1016/j.agwat.2024.109071, 2024.

Wang, Y., Shi, L., Hu, Y., Hu, X., Song, W., and Wang, L.: A comprehensive study of deep learning for soil moisture prediction, Hydrol. Earth Syst. Sci., 28, 917–943, https://doi.org/10.5194/hess-28-917-2024, 2024.

Wang-Erlandsson, L., Bastiaanssen, W. G. M., Gao, H., Jaegermeyr, J., Senay, G. B., van Dijk, A. I. J. M., Guerschman, J. P., Keys, P. W., Gordon, L. J., and Savenije, H. H. G.: Global root zone storage capacity from satellite-based evaporation, Hydrol. Earth Syst. Sci., 20, 1459-1481, https://doi.org/10.5194/hess-20-1459-2016, 2016.

Wigneron, J. P., Kerr, Y., Waldteufel, P., Saleh, K., Escorihuela, M. J., Richaume, P., Ferrazzoli, P., de Rosnay, P., Gurney, R., Calvet, J. C., Grant, J., Guglielmetti, M., Hornbuckle, B., Mätzler, C., Pellarin, T., and Schwank, M.: L-band microwave emission of the biosphere (L-MEB) model: Description and calibration against experimental data sets over crop fields, Remote Sens. Environ., 107, 639–655, https://doi.org/10.1016/j.rse.2006.10.014, 2007.

Zhang, R., Nayak, A., Houtz, D., Watts, A., Soltanaghai, E., and Alipour, M.: Evaluation of soil moisture retrievals from a portable L-band microwave radiometer, Remote Sens., 16, 4596, https://doi.org/10.3390/rs16234596, 2024.

Zhao, T., Shi, J., Entekhabi, D., Jackson, T. J., Hu, L., Peng, Z., Yao, P., Li, S., and Kang, C. S.: Retrievals of soil moisture and vegetation optical depth using a multi-channel collaborative algorithm, Remote Sens. Environ., 257, 112321, https://doi.org/10.1016/j.rse.2021.112321, 2021.

Zhong, Y., Wei, Z., Miao, L., Wang, Y., Walker, J. P., and Colliander, A.: Downscaling passive microwave soil moisture estimates using stand-alone optical remote sensing data, IEEE Trans. Geosci. Remote Sens., 62, 1–19, https://doi.org/10.1109/TGRS.2024.3386967, 2024.